THESIS FOR THE DEGREE OF LICENTIATE OF ENGINEERING

3D Reconstruction of Porous and Poorly Conductive Soft Materials using FIB-SEM Tomography

CECILIA FAGER

CHALMERS

Department of Physics
CHALMERS UNIVERSITY OF TECHNOLOGY
Gothenburg, Sweden 2018

3D Reconstruction of Porous and Poorly Conductive Soft Materials Using FIB-SEM Tomography

CECILIA FAGER

Division of Eva Olsson Group
Chalmers University of Technology
Gothenburg, Sweden - 412 96
Telephone + 46 (0)31-7723334
cecilia.fager@chalmers.se

Cover:
The figure on the cover shows the internal microstructure within a porous polymer film intended for controlled drug release (left) SEM BSE 3D image stack with one outlet pore marked in pink, (top middle) 3D reconstruction of the porous network existing in the left image with the same outlet pore marked in pink, (right) 3D reconstruction of the path for the outlet pore marked in pink and (bottom middle) transparent SEM BSE 3D image stack with a pore path marked in red.

Printed by:
Chalmers Reproservice
Gothenburg, Sweden 2018

3D Reconstruction of Porous and Poorly Conductive Soft Materials Using FIB-SEM Tomography

CECILIA FAGER
Department of Physics
Chalmers University of Technology

Abstract

Focused ion beam combined with scanning electron microscope (FIB-SEM) is a powerful tool that can be utilised to reveal the internal microstructure of materials. It basically uses ions to make cross-sections with high precision and electrons to image the cross-section surface with high spatial resolution. In addition to revealing the internal microstructure, FIB-SEM can be used to perform a sequential slice and image procedure which, after some data processing, can result in a 3D reconstruction of the microstructure, also denoted as FIB-SEM tomography. Focused ion beam tomography is a well-established procedure since 1987. It has been successfully applied to a variety of well conductive materials. However, to perform FIB-SEM tomography on ion and electron beam sensitive as well as poorly conductive soft materials is still challenging. Some of the common challenges are cross-sectioning artefacts, shadowing-effects and charging. The presence of pores adds additional challenges. Fully dense materials provide a planar cross-section while pores expose surface area beneath the planar cross-section surface as well. The sub-surface pore information and the varying intensity from the sub-surface areas give rise to intensity overlaps which complicates the data processing. Several solutions to overcome these challenges have been reported. Examples are milling and imaging at low beam energies and specimen preparations. However, the ultimate aim is to examine porous and poorly conductive soft materials as close to their original state to avoid introduction of artefacts.

The aim of this work was to develop a general protocol for optimisation of FIB-SEM tomography parameters for porous and poorly conductive soft materials. The optimised parameters include the energies and currents of the ion and electron beams, reduction of shadowing-effects, choice of electron detector and selection of method for charge neutralisation. In addition, a new self-learning binarisation algorithm is introduced to enable an automatic separation between pores and matrix. The binary data have been used to visualise the interconnectivity in 3D of individual pore paths through phase separated polymer films. The optimised protocol for FIB-SEM tomography is applicable to a variety of porous and poorly conductive soft materials.

The porous and poorly conductive soft materials in these studies were leached phase separated polymer films intended for controlled drug release coatings in pharmaceuticals. The porous microstructure within the films acts as transport path for the drug. In this work, the complex microstructure has been visualised in 3D. In addition, 3D visualisation of the shortest, intermediate and longest paths through the films, based upon tortuosity calculations, have been performed as well.

Keywords: focused ion beam, scanning electron microscopy, tomography, 3D, insulating material, interconnectivity, polymer film

PREFACE

The research presented in this thesis was carried out in the division of Eva Olsson Group in the Department of Physics, Chalmers University of Technology, Gothenburg, Sweden during the periods of November 2015 – October 2018, under the supervision of Prof. Eva Olsson and assistant supervisors Dr. Christian von Corswant, Dr. Niklas Lorén and Prof. Aila Särkkä.

This work was founded by the Swedish Foundation of Strategic Research.

The following book chapter and papers are included in this thesis:

Book chapter. **Soft Materials and Coatings for Controlled Drug Release**
Nanotechnologies in Preventive and Regenerative Medicine an Emerging Big Picture. V. Uskokovic and D. P. Uskokovic
C. Fager and E. Olsson
Netherlands: Elsevier. 2018, 244-259.

Paper I. **3D Reconstruction of Microstructure Using Optimised FIB-SEM Tomography Parameters for Porous and Poorly Conductive Soft Materials.**
C. Fager, M. Röding, A. Olsson, C. von Corswant, N. Lorén, A. Särkkä and E. Olsson
Manuscript intended for Microscopy and Microanalysis

Paper II. **3D Visualisation of Individual Transport Paths in Controlled Drug Release Films using FIB-SEM Tomography**
C. Fager, S. E. Barman, M. Röding, A. Olsson, C. von Corswant, N. Lorén, A. Särkkä, H. Rotzén and E. Olsson
Manuscript intended for International Journal of Pharmaceutics

My contribution to the appended manuscripts:

Book chapter: I wrote the book chapter in discussion with my co-author Prof. Eva Olsson.

Paper I: I did all the microscopy work, carried out the evaluation in discussion with my co-authors and wrote the paper.

Paper II: I did all the microscopy work, carried out the evaluation in discussion with my co-authors and was the main author of the paper.

In addition to the above book chapter and papers, I have contributed to the following work, which is not included in this thesis:

Fabrication and Characterization of Plasmonic Nanopores with Cavities in the Solid Support
B. Malekian, K. Xiong, G. Emilsson, J. Andersson, **C. Fager**, E. Olsson, E.M. Larsson-Langhammer and A.B. Dahlin
Sensors 2017, **17** (6), 1-11

Cecilia Fager
Gothenburg, September 2018

Acknowledgments

Dear Prof. Eva Olsson, I would like to perform my express gratitude to you. You are always there to support me, no matter where in the world you are. You always take your time to guide me through my PhD journey and that is a privilege to me. Thank you for being you and for these years that have passed, I am truly looking forward to the upcoming exciting years.

I would like to thank my co-supervisors, Dr. Niklas Lorén (RISE and adj. Prof. in EOG), Prof. Aila Särkkä (Dept. of Mathematical Sciences) and Dr. Christian von Corswant (AstraZeneca). Dr. Niklas Lorén, I really enjoy our discussions and I am very thankful for the positive energy you gave me especially during the final parts of the writing of my licentiate thesis. Prof. Aila Särkkä, you are one of the most humble humans I have met. You always share your supporting smile and expertise. Dr. Christian von Corswant, I truly appreciate our fruitful discussions and that I know that you are always there to support me.

Furthermore, I would like to acknowledge AstraZeneca and especially thank Dr. Anna Olsson for her expertise and valuable input to this work.

I would like to acknowledge the Swedish Foundation for Strategic Research (SSF) for funding this PhD project. To all of my colleagues within this SSF project I would like to say that it is always a true pleasure to work with you. Sandra Barman Eriksson (Dept. of Mathematical Sciences), my academic sister, it is always fun and efficient to work together with you. These are two important ingredients for making a great team. Dr. Magnus Röding (RISE), the passion I share for electron microscopy, you share for computations and data processing, I truly enjoy working with you.

My colleagues within Eva Olsson Group, you are the definition of perfect colleagues to me. We always share laughter and supporting each other. The wide variety of expertise within the EOG is one of many reasons that will keep us breaking new scientific ground. I want to give a thanks to Dr. Andrew Yankovich for always asking questions that makes me think twice, Dr. Ludvig de Knoop for always making me smile with your jokes, Dr. Torben Pingel Nilsson for being a great office mate, Dr. Lunjie Zheng for always supporting me and my former EOG colleague Dr. Norvik Voskanian for always keeping me on my toes.

I would also like to give a huge thanks to my colleagues in the group of Materials Microstructure for filling the lunch breaks with laughter where I always learn something new.

Dr. Stefan Gustafsson, Dr. Katarina Logg and Dr. Reza Zamani from CMAL (Chalmers Materials Analysis Laboratory), thank you all for sharing your amazing skills and always being there to help whenever challenges appear by the electron microscopes or elsewhere. I would also like to thank the former manager of CMAL, Dr. Anders Kvist, for helping me throughout these years. I will also direct a huge thanks to Ola Löfgren who have solved all my computer challenges, especially when my computer crashed during writing this thesis.

Last I would like to send my love to my dad, mom and brother who are always there to catch me whenever I fall (yes, we all do that sometimes) as well as share my happiness when those indescribable electron microscopy moments appears after years of well invested time (that is true happiness to me).

The best part is that this story continues and I am so lucky to work close with all of you amazing and skilled human beings.

Table of Contents

Chapter 1

- "Something unknown is waiting on being known"

INTRODUCTION

BACKGROUND

The correlation between structures and properties of materials is of great importance to understand in order to optimise materials for their applications. One way to increase the understanding of materials properties is to visualise their structures in three-dimensions (3D). There exist several well established imaging techniques such as light microscopes and electron microscopes. The choice of which analysis technique to utilise depends on various factors such as what type of material and desired resolution of the structures. If the aim is to image structures at the larger length scale, optical microscopes are preferred. However, if the structures are at the smaller length scale, electron microscopes would be the choice (Subramaniam, 2005). The conventional scanning electron microscope (SEM) is imaging materials by raster an electron beam over the material surface. Depending on the desired information, different detectors can be utilised. An SEM has one main criteria that needs to be fulfilled which is to operate under vacuum, hence, liquid containing materials are not suitable to be imaged in an SEM. However, the development of the SEM has resulted in that gas can be allowed into the chamber. This instrument is known as a low vacuum – scanning electron microscope (LV-SEM). The LV-SEM can be used to image soft materials such as polymers (Stokes *et* al., 2008; Jansson *et* al., 2013).

Moreover, when the interest is to reveal and image the internal microstructure of a material, a focused ion beam (FIB) combined with a scanning electron microscope (SEM) can be utilised. It basically uses the ions to remove material with high spatial precision and create cross-section. The electrons are utilised to image the revealed cross-section surface with high spatial resolution. The FIB with a liquid-metal-ion-source has been around since 1979 and was initially used as a tool for specimen preparation (Seliger *et* al., 1979). However, further development of the instrument resulted in a variety of applications and one of them was FIB tomography (Kirk *et* al. 1987). In a FIB, both the milling and the imaging are performed using the ion beam. It was quickly noted that the ion beam damaged the surface even during imaging. The next generation of instruments introduced the combination of FIB and SEM. This provided the opportunity to image without damaging using the electron beam (Inkson *et* al., 2001). The FIB-SEM could now also be used for 3D data acquisition using the ion beam for high precision serial sectioning and the electron beam for imaging with high spatial resolution.

It should be pointed out that FIB-SEM tomography is routinely applied to highly conductive metals and ceramics. However, for soft materials such as biological specimens in their natural state, 3D FIB-SEM data acquisition is still a challenge. One common factor for

biological specimens has been that they all need specimen preparation that includes several steps in order to withstand the vacuum in FIB-SEMs (Heymann *et* al., 2006). From previous findings, several examples of specimen preparations have resulted in successful imaging of poorly conductive materials. If a soft material contains high amount of water, examination under cryo-conditions can be preferable (Dubochet *et* al., 1988). During cryo, the specimen is frozen during a specimen preparation prior to the imaging. Another example is if the contrast is poor while imaging with SEM, a specimen preparation involving fixation using heavy metals can be utilised (Seligman *et* al., 1966; Tanaka *e*t al., 1984; Deerinck, *et* al., 2010). The heavy metals enhance the contrast in the soft material and the SEM imaging can be performed. Even though these specimen preparations have been successfully applied, the materials are not examined during their natural state which can introduce artefacts.

Porous and poorly conductive soft materials are for example used in the pharmaceutical industry as coatings for controlled drug release (Lecomte *et* al., 2003; Siepmann *et* al., 2007; Siepmann *et* al., 2008). The desired release of an oral pharmaceutical product is an as optimal drug therapy as possible. Tailoring drug release utilising drug cores coated with phase separated polymer films is a well-established procedure and research have been performed within this field over many years. The research has the last decades resulted in an increased performance of these types of drug delivery systems due to a more controlled chemistry behind the manufacturing process (Marucci *et* al., 2013).

AIM OF THE WORK

The aim of this work was to develop a general protocol for optimisation of FIB-SEM tomography parameters for porous and poorly conductive soft materials. The optimised parameters included the energies and currents of the ion and electron beams, reduction of cross-sectioning artefacts such as curtaining and redeposition, shadowing-effects, choice of electron detector and selection of method for charge neutralisation. In addition, a new self-learning binarisation algorithm was introduced to enable an automatic separation between pores and matrix. The binary data were also used to visualise the interconnectivity in 3D of individual pore paths through phase separated polymer films intended for controlled drug release.

Chapter 2

- "No one is you, that is your power"

CONTROLLED DRUG RELEASE USING POLYMER COATINGS

Controlled drug release coatings have been around for more than 50 years and their performance has increased significantly since their beginning partly due to a more controlled chemistry during the fabrication (Rhodes *et* al., 1998). The overall goal of a pharmaceutical product is to obtain an optimum therapeutic as well as tailored treatment for its cause (Klein, 2002). In order to achieve this overall goal, a combination of an effective active pharmaceutical ingredient (API) and a tailored controlled release (CR) rate is required (Hutton *et* al., 1992). In addition, a minimisation of the total amount of drug that is needed and elimination of plausible side effects (Edsbäcker *et* al., 2003; Anderson *et* al., 1999). There exist different aspects that needs to be considered in order to obtain the specific drug release behaviour that is envisioned. One aspect that is of great importance to be considered is the gastrointestinal tract (GI). It is where the drug release will occur and be further directed to the targeted location (Gruber *et* al., 1987). Different pH-values exists throughout the GI tract. It does also need to be pointed out that the pH-values within the GI tract also vary depending on fed or starving condition. The different pH values need to be taken into account when selecting a soft material as controlled release coating. This is due to that different materials have different solubilities within different pH-values.

Immediate release (IR) formulations gives a rapid release of the drug from the formulation. IR can be utilised for several formulation systems such as capsules and pellets by adding a coating that surrounds the drug and dissolves fast in the surrounding medium. The IR formulations are desired whenever the drugs have a wide therapeautic window and a long half-time in the body (Divoll *et* al., 1983). The IR formulations can also be utilised as an oxygen barrier since some drugs are sensitive to the presence of oxygen. (Felton *et* al., 2006; Felton, 2007).

Controlled release (CR) formulations can be used when a release of a drug needs to occur during a longer period of time (Rhodes *et* al., 1998). There exist two major types of CR formulations which are based upon either coating a drug core with a film or dispersing a drug within a matrix material.

The source of the polymers can be either natural or synthetic. A common constitute of these types of films is cellulose derivative (Langer *et* al., 1983). One major advantage with cellulose is that it is non-toxic and harmless. Cellulose derivatives are modified cellulose, and they possess a great variability since they can be modified by adding substitution groups to the backbone. Therefore, a two-component film could consist of one hydrophilic cellulose and one hydrophobic cellulose, depending on the added substitution groups.

SOFT MATERIALS FOR CONTROLLED DRUG RELEASE

It was mentioned in the previous section that there exist two major types of CR formulations, where one coating surrounds a drug core and where the drug is dispersed within a matrix. This section gives an overview of polymer sources for CR formulations. Depending on the source the polymer is produced from, it is either denoted as natural polymers or synthetic polymers (Langer *et* al., 2003). Some advantages of natural polymers are that they are highly accessible since their source are for example plants. The synthetic polymers are synthesised in a controlled way which gives better control of instance molecular weight distribution. This can be used to more carefully tailor the drug release.

Additional components can be added to the CR formulations. These additional components are called excipients. As already described, one excipient can be the coating that is utilised to control the drug release from a drug core. Pores within a coating can be added by addition of so called porogens which can be utilised to affect the release mechanisms (Sakellariou *et* al., 1995). Another important aspect is storage of the final pharmaceutical product. It is of great importance that agglomeration due to stickiness of the pharmaceutical does not occur. Hence, antiadherents could be added as an excipient which prevents the pharmaceutical product from agglomerating. If the film flexibility needs to be improved, plasticizers can be added. In addition, if a colour coating is requested, pigments can be added as well.

POLYMER PHASE SEPARATION

The procedure of how to coat a drug core with a phase separated polymer film, intended for controlled drug release, is a well-established procedure (Siepmann *et* al., 2008). The phase separation kinetics during the manufacturing process is controlling the formed microstructure within the films. This microstructure acts as the transport path for the drug. One way to coat the drug core with the phase separated polymer film is by spraying a solution onto the drug core. The solution consists of the two immiscible polymers solved by a solvent. When the solvent is evaporating, the phase-separation between the two immiscible polymers occurs (Jones *et* al., 1999). There are several ways of going from a one-phase solution (two immiscible polymers are dissolved with a solvent) to a two-phased solution (two immiscible polymers have been phase separated). This will be explained by the following three examples. One way to induce phase separation if to change the temperature, see Figure 1a). When the temperature is lowered, the one-phase solution turns into a two-phase solution. Another way to turn a one-phase solution into a two-phased solution is to evaporate the solvent, see Figure 1b). A third way could be to increase the degree of polymerisation, see in Figure 1c).

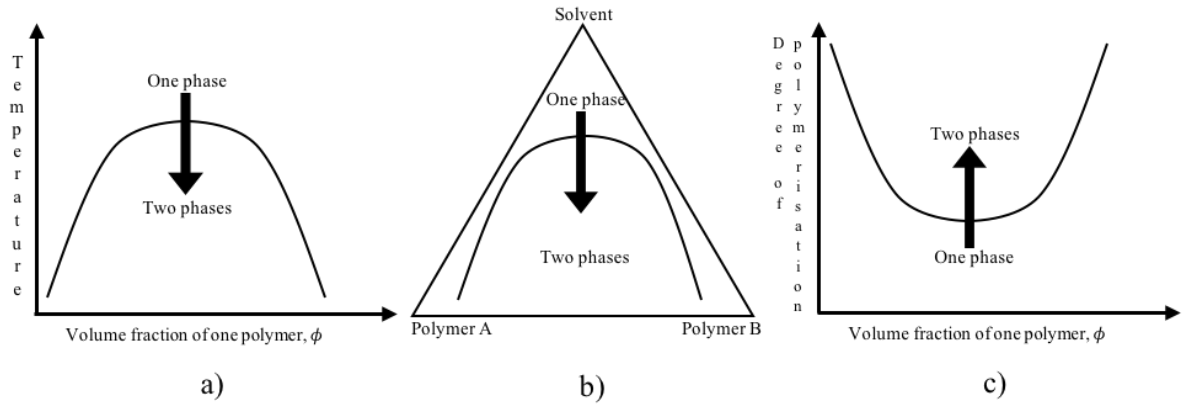

Figure 1. Illustration of three different factors that can cause phase separation where a) shows that cooling of a solution of two immiscible polymers with a solvent result in a phase separation. b) shows that solvent is evaporating can cause phase separation occurs and c) shows that a higher degree of polymerisation causes phase separation (adapted from Jones *et* al., 1999).

EC/HPC PHASE SEPARATED POLYMER FILMS

In literature, it has been shown that cellulose (EC) provides a coherent film and is therefore often selected to be added as the majority polymer in the polymer solution utilised for coatings for controlled drug release (Sakellariou *et* al., 1995; Lecomte *et* al., 2003). Hence, the EC is defined as the matrix material of the films. Hydroxypropyl cellulose (HPC) is water insoluble and is forming a porous microstructure within the films upon contact with water, hence defined as the pore former. The solvent utilised to dissolve the two immiscible polymers can for example be ethanol. The polymer phase separation is initialised by the ethanol evaporation. As a consequence of the evaporation, segregative phase separation occurs and EC-rich and HPC-rich phases are formed. In a certain polymer concentration regime,
bicontinuous structures are formed. The phase separation mechanism resulting in bicontinuous structures is called spinodal decomposition. The film structure is kinetically trapped by a high film viscosity which is reached at a certain ethanol concentration during the evaporation (Marucci *et* al., 2013). By immerging the phase separated polymer films into water, the HPC leaches out. This creates a porous microstructure within the EC matrix (Siepmann *et* al., 2007). The porous microstructure is the transport path for the drug.

It has been shown that the release properties of the EC/HPC films can be varied by varying different factors. For example, process parameters during manufacturing as well as the molecular weights for the polymers (Marucci *et* al, 2013; Andersson *et* al, 2013). It was found that an increased molecular weight resulted in a decreasing film permeability (Andersson *et* al., 2018, Andersson *et* al., 2016). In addition, varying the polymer volume percentage of the two polymers shows that a percolation onset exists around 22 volume percentage of HPC (Marucci *et* al., 2009). The film permeability was lower below the 22 volume percentage and higher above the 22 volume percentage.

Different techniques have been utilised to investigate the release properties of phase separated polymer films. For example, a diffusion cell has been utilised to investigate the release mechanisms (Marucci *et* al., 2009). It was found that the release mechanism depended on the initially amount of water soluble polymer. In addition, the release mechanism changed from osmotic pumping to diffusion as the initial amount of water soluble polymer was increased. Furthermore, Low-Vacuum Scanning Electron microscopy (LV-SEM) provided new, valuable insights of the water transport through the phase separated EC/HPC polymer films (Jansson *et* al., 2013). This method provided the possibility to visualise the water transport and the film microstructure simultaneously.

Chapter 3

- "Let your smile change the world"

EXPERIMENTAL

This chapter provides an overview of the basic principles of a FIB-SEM instrument. It gives a brief introduction to the ion beam milling and its challenges. In addition, electron beam imaging is briefly described as well as common problems encountered while imaging poorly conductive soft materials. The preparation of the studied phase separate polymer films is described as well as the FIB-SEM tomography set-up.

MATERIALS

MANUFACTURING OF PHASE SEPARATED POLYMER FILMS

Free standing phase separated polymer films were prepared from a solution. The solution consisted of ethyl cellulose (EC) (Ethocel™ Standard Premium with viscosity grade 10 cP from Dow Wolff Cellulosic GmbH in Germany) and hydroxypropyl cellulose (HPC) (Klucel® Pharm HPC with viscosity grade LF from Ashland in USA) dissolved with 95% ethanol (Marucci *et* al., 2009; Jansson *et* al., 2013). The films were produced by spraying the solution onto a rotating drum using a nozzle that moved from side to side. Figure 2 shows the moving spraying nozzle, the spray zone as well as the rotating drum.

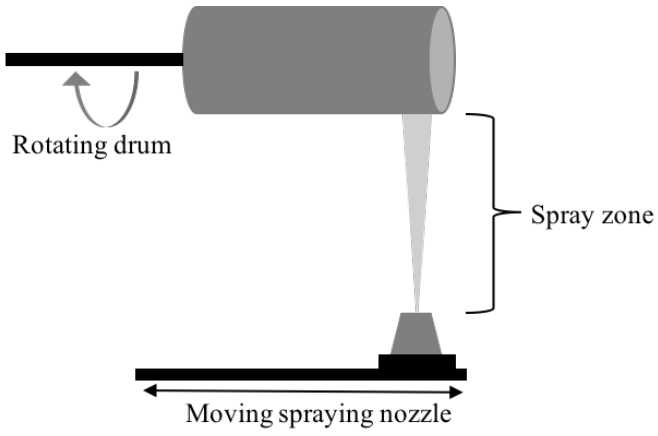

Figure 2. Schematic illustration of the manufacturing process of the phase separated polymer films. The polymer solution was sprayed onto a rotating drum using a moving spraying nozzle.

The phase separated polymer films was removed from the drum after the spraying processes. Several films were produced by vary the volume percentage between EC and HPC. The films were named after the added volume percentage of HPC, hence HPC22 had 22 volume percentage of HPC and 78 volume percentage of EC. Three films have been examined in this work which are HPC22, HPC30 and HPC45. As mentioned in previous section, EC is added as the main component due to EC provides a coherent coating. The HPC was added as the pore former. The HPC was removed by leaching the films in water. The purpose of the leaching was to reveal the porous microstructure. The leaching of the films was done by cutting squares of 0.5 cm x 0.5 cm from the original films. The small squared film specimens were immerged in 700 ml stirred deionised water at room temperature for 24 hours. The deionised water was changed two times. Finally, the films were air-dried and later on stored in a desiccator. Figure 3 shows a sketch of leached porous film where the different features of the film are marked. The grey colour represents the EC matrix while the white represents the porous microstructure. The dried leached films were mounted onto an alumina stub with sticky carbon tape. Followed by deposition of a few nm thin palladium coating onto the specimen surfaces to reduce the charging effects. The EMITACH K550X Palladium Sputter was used with coating current 25 mA, coating time 3 minutes and during rotation of the specimen holder.

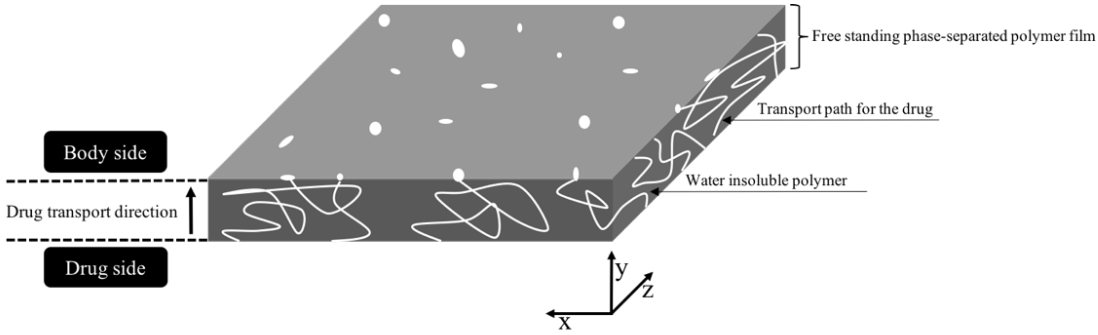

Figure 3. Schematic overview of the leached porous polymer film. The grey colour represents the porous ethyl cellulose (EC) matrix while the white represents the porous microstructure.

ANALYTICAL METHODS

3D reconstruction of porous and poorly conductive soft materials using a focused ion beam (FIB) combined with a scanning electron microscope (SEM) involves several steps. This section describes the basics of a FIB-SEM instrument as well as the interactions between the ion and electron beams with the specimen surface. Several challenges are encountered while working with porous and poorly conductive soft materials in a FIB-SEM, some of them are briefed as well.

FIB-SEM DUAL BEAM MICROSCOPY

A focused ion beam (FIB) combined with a scanning electron microscope (SEM) provides the possibility to reveal and image the internal microstructure of materials. The FIB-SEM utilises the focused ion beam to make cross-sections with high precision and the electron beam to image the internal microstructure with high spatial resolution (Bassim *et* al., 2014; Cantoni *et* al., 2014). The FIB-SEM have one ion column and one electron column, where upon the ion and electron beams are focused separately during vacuum conditions.

The FIB-SEM instrument utilised throughout this work was a Tescan GAIA3 (Tescan, Czech Republic). The FIB-SEM tomography software from TESCAN was utilised to perform the slice and image procedure. The instrument was equipped with a gas injection system (platinum and carbon). The coincidence point of the ion and electron beam was at 55°, see Figure 4 for the FIB-SEM set-up.

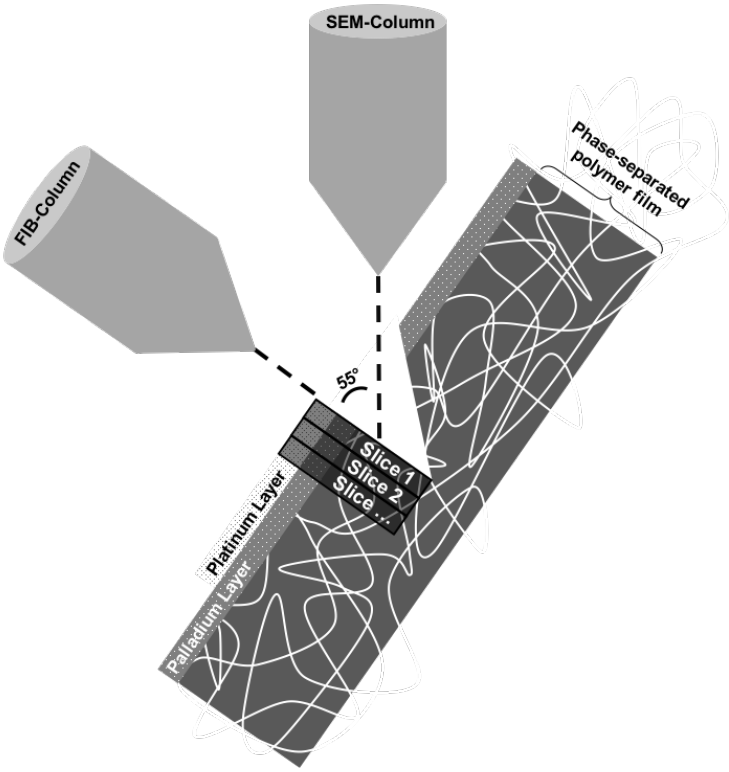

Figure 4. The setup of focused ion beam combined with scanning electron microscope and the specimen. The incident angle of the electron beam and the ion beam is 90˚ and 55˚, respectively, in order to perform milling an imaging immediately after each other.

ION BEAM MILLING

Ions can be utilised for removing material from a specimen with high precision, depositing material onto the specimen as well as imaging the specimen surface. However, ions are significantly more massive compared to for example electrons, which thus needs to be kept in mind when imaging with ions. Imaging with ions may sputter away and thus damage the specimen surface (Giannuzzi *et* al., 2005). A sputtering process occurs if the kinetic energy of the ions is sufficient to overcome the surface binding energy of the surface atoms in the specimen. Figure 5 shows a schematic illustration of the interaction between an ion and the specimen surface (Nastasi *et* al., 1996). This sputtering process is referred to as milling in the literature. The milling process can be controlled, hence be performed with high precision (Giannuzzi *et* al., 2005). It has been shown that cross-sectioning artefacts such as curtaining and redeposition can be reduced with fine tuned ion beam current and energy (Walley *et* al., 1971; Suzuki, 2002; Drobne *et* al., 2007).

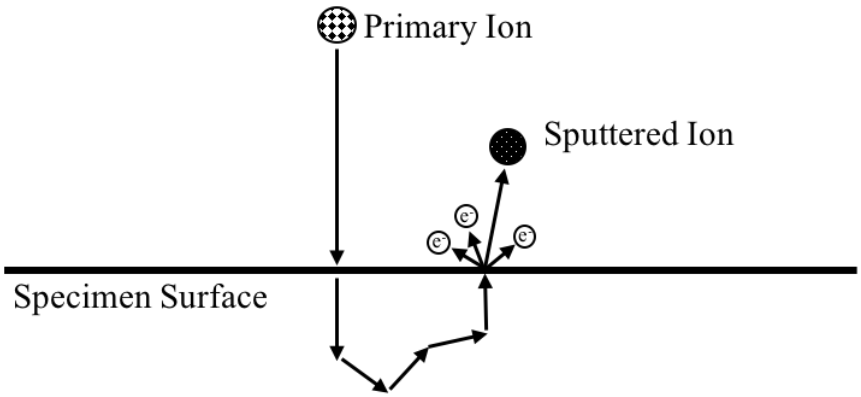

Figure 5. Schematic illustration of ion-solid interaction between incident ion and specimen surface resulting in sputtered ion from the specimen (adapted from Nastasi *et* al., 1996).

CROSS-SECTIONING ARTEFACTS

Ion beam milling can cause cross-sectioning artefacts such as curtaining or redeposition (Giannuzzi *et* al., 2005). Curtains are vertical lines seen in the cross-section surface caused by the ion beam. Different hardness within a material or thickness can cause different ion milling rates which can cause curtaining. Redeposition is removed material that is still in the chamber and deposit onto the cross-section surface. Previous work has shown that deposition of a platinum coating onto the specimen can be used to reduce the curtaining effect (Walley *et* al., 1971; Suzuki, 2002; Drobne *et* al., 2007). Platinum gas precursor is injected into the chamber. The precursor is cleaved by the ion beam. This results in deposition of platinum under the ion beam. The platinum coating provides a homogenous surface which give rise to a more constant milling rate. It has also been shown that curtaining and redeposition can minimised by reduced milling rates (Giannuzzi *et* al., 2005).

ELECTRON BEAM IMAGING

Electrons can be utilised to image as well as deposit material onto a specimen surface. The incident electrons interact with the specimen surface which results in an interaction volume, see Figure 6. This interaction produces different signals that can be detected with suitable detectors for the different signals (Goldstein, 2003). The signals are for example backscattered electrons, secondary electrons and characteristic X-rays. Figure 6 shows a cross-section with the interaction volume and different types of signals. The backscattered electrons are produced when a primary electron interacts with an atom from the specimen. The interaction causes the path of the primary electron to deviate from its original path and thus leaving the specimen as a backscattered electron. The secondary electrons are derived from when the primary electrons are emitting electrons from the specimen. Characteristic X-rays are produced when electrons from the specimen that are tightly bonded are ejected from the inner shell. This creates an electron hole which is filled with an electron from a higher energy shell. The energy difference between the shell above and the shell below is released in the form of emitted characteristic X-rays.

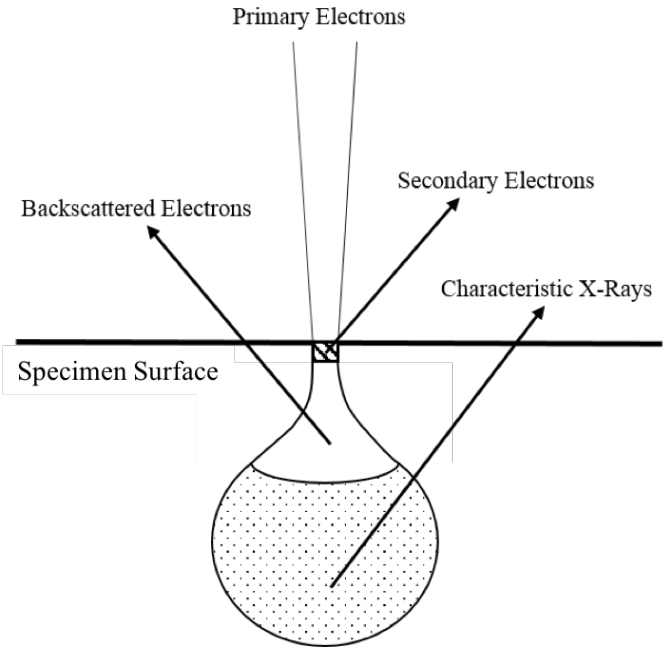

Figure 6. Schematic illustration of the interaction between the electron beam and the specimen (adapted from Goldstein, 2003).

IMAGING CHALLENGES

Two common problems encountered when imaging a cross-section surface utilising an electron beam are shadowing-effects and charging. The shadowing-effects are caused by the surrounding material of the cross-section. In order to eliminate these shadowing-effects, trenches on each side and in front of the cross-section (a U-shape) can be milled with the ion beam. Figure 7 shows a schematic overview of the different steps involved to establish the U-shape. The initial step was to deposit a thin platinum coating on the specimen surface to reduce the curtaining effect. The platinum deposition was done within two steps, first by deposition with the electron beam and then by the ion beam, see number 1 in Figure 7. A cross-section was milled in order to reveal the internal porous microstructure, see Figure 7 number 2, followed by milling narrow trenches on each side of the cross-section, see number 3 in Figure 7. In order to reveal the full cross-section surface, a bigger trench in front of the cross-section was milled, see number 4 in Figure 7. Following, platinum was deposited in two squares where fiducial markers (used to prevent drifting) was milled into, see number 5 in Figure 7. The last step was to clean the cross-section from curtains and redeposition, see number 6 in Figure 7. This was also the starting point of the slice and image procedure.

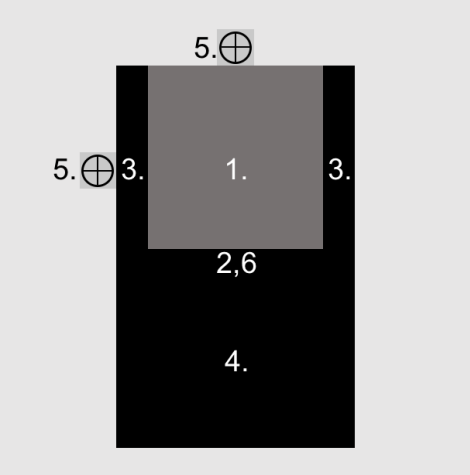

Figure 7. Schematic overview that shows the different steps required to establish a U-shape. Number 1 represents deposition of a protective platinum coating. Number 2 shows the location of the first cross-section of the U-shape. Number 3 represent the narrow trenches of the U-shape. Number 4 shows the big trench that revealed the full cross-section surface. Number 5 shows the location of the fiducial markers for the FIB and the SEM. Number 6 is the starting point of the slice and imaging procedure.

From previous findings, it is known that no charging of poorly conductive materials is present when the number of primary electrons impinging on the surface is roughly equal to the number of electrons emitted from the specimen surface, i.e. the total number of backscattered electrons (BSE, η) secondary electrons (SE, δ) (Goldstein, 2003). The beam energy influences the ratio between the number of incoming electrons and the emitted electrons and therefore needs to be tuned to achieve the condition of no charging. There are two cross-over points, E_1 and E_2, where the primary beam energy gives an electron yield equal to 1, see Figure 8. For soft materials, the low energy cross-over point occurs in the energy range of 0.5 keV – 2 keV and the high energy

cross-over point at 2 keV - 5 keV (Goldstein, 2003). At low energy below the first cross-over point, E_1, there is a negative charge accumulation. At energies between the two cross-overs there is a positive charge accumulation and above the second cross-over point, E_2, there is a negative charge accumulation.

Furthermore, when imaging conductive materials with low electron beam energy, secondary electron detector is often selected (Goldstein, 2003). However, when charging occurs, the secondary electrons are much more affected by the charging because of their low kinetic energy, < 50eV than backscattered electrons. Therefore, BSE is preferred when imaging of poorly conductive materials.

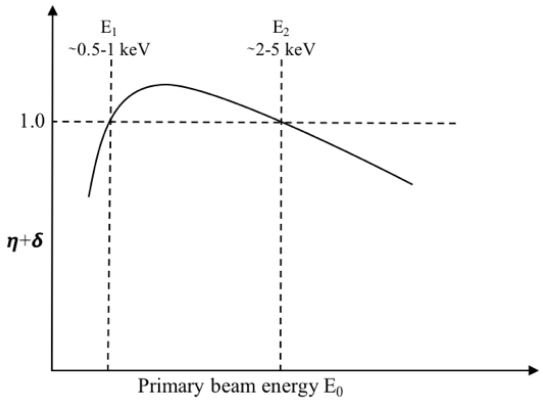

Figure 8. Schematic illustration of the total emission of backscattered electrons (η) and secondary electrons (δ) as a function of incident beam energies. The lower cross-over point is E_1 and the upper cross-over point is E_2 (adapted from Goldstein, 2003).

Another approach to reduce charging while imaging poorly conductive specimens with electrons is to operate the FIB-SEM in a low-vacuum condition. It reduces charging through ionisation of the gas molecule. The ions neutralise the accumulated charges at the surface (Robinson, 1975; Moncrieff *et* al., 1978; Stokes, 2008). This approach can however not be used simultaneously using the ion beam. In addition, it has been shown that a localised discharge can be achieved by injecting a nitrogen gas using a gas injection system (Schulz *et* al. 2009). This approach limits the area of lower vacuum and the area of interest can be imaged with reduced charging.

As already mentioned, poorly conductive soft materials have to be prepared before they can be inserted into the FIB-SEM for tomography. Previous work has shown that an increase of the concentration of heavy metals in the specimen reduce charging. The heavy metals increases the conductivity of the poorly conductive specimens (Seligman *et* al., 1966; Tanaka *et* al., 1984; Deerinck *et* al., 2010). In addition, it has been shown that a combination between low electron beam energy, osmium-fixed specimens and backscattered electron detector can be used to image poorly conductive specimens. The low electron beam energy reduced the charging and the osmium-fixation enhanced the contrast as well as increased the BSE yield. (Harris *et* al. 1976; Holzer *et* al. 2004; De Winter *et* al., 2009).

DATA SEGMENTATION

3D reconstruction of materials using FIB-SEM tomography is done by reconstructing binary 2D image stacks. Binarisation of the 2D image stacks are usually performed by aligning the image stack, followed by cropping and segmentation (Jorgensen *et* al., 2010). Global thresholding is one common way to perform the segmentation (Efford *et* al., 2000). In global thresholding, a prechosen threshold value is determined to distinguish the two phases. If the grey value of a pixel is below the prechosen threshold, it belongs to one of the phases and if it is above, it belongs to the other phase. However, the segmentation of porous materials is complex. The 2D image of the cross-sections does not only contain information about the cross-section surface but also information from inside the pores (Zils *et* al., 2010; Schulenburg *et* al., 2011). This leads to overlapping intensities where global thresholding is not sufficient as segmentation method. Even more advanced segmentation algorithms such as local thresholding have been presented but does not solve this complex segmentation problem (Blayvas *et* al., 2006; Thiedmann *et* al., 2011). An approach that does consider this is the local threshold backpropagation method (Salzer *et* al., 2012). It is based on detection of structures that disappear and subsequent thresholding backpropagation.

Chapter 4

- "The master was once a beginner"

RESULTS

3D reconstructions of porous and poorly conductive soft materials have been done by developing a protocol of how to fine tune FIB-SEM parameters. In addition, a self-learning binarisation algorithm has been developed to solve the segmentation problem. The interconnectivity of individual porous paths have been visualised in 3D as well. The protocol of how to fine tune the ion beam parameters is presented first. The fine tuned ion beam parameters reduces cross-sectioning artefacts such as curtaining and redeposition. The following section presents the protocol of how to fine tune the electron beam parameters. This involves establishment of a U-shape to eliminate shadowing-effects. In addition, charging has been reduced by deposition of a platinum coating and a method of charge neutralisation. The segmentation problem for binarisation of the 2D image stacks has been solved by a new self-learning binarisation algorithm. Three leached phase separated polymer films, intended for control drug release with varied porosity have been examined.

OPTIMISATION OF ION BEAM MILLING

REDUCTION OF CROSS-SECTIONING ARTEFACTS

The protocol for optimisation of ion beam milling parameters to reduce cross-sectioning artefacts, such as curtaining and redeposition, included deposition of a protective platinum coating and fine tuned ion beam parameters. After the platinum coating had be deposited, the ion beam parameters were fine tuned. The optimisation of the milling parameter was carried out by tuning the ion beam energy and current. The conclusion was that the cross-sectioning artefacts could all be avoided at 30 keV provided that the ion beam current was fine tuned. The currents were optimised by following experimental approach. When milling the largest trench, a high current as possible without causing too much cross-sectioning artefacts was required in order to achieve a time efficient milling. The tuning of the highest ion beam current was started using 20 nA followed by a stepwise increase to find the optimised current, which was 40 nA in this case. Cross-sectioning artefacts were present here. However, these were removed upon following steps during the cleaning of the cross-section where lower beam currents were used. The other milling operations were optimised with same approach, but started at lower currents. The specimen surface was examined after each milling current to choose the highest current that did not cause cross-sectioning artefacts. The ion beam parameters used for slicing were 1 nA and 30 keV.

OPTIMISATION OF ELECTRON BEAM IMAGING

REDUCTION OF SHADOWING-EFFECTS AND CHARGING

The protocol to optimise the electron beam imaging of porous and poorly conductive soft materials involved elimination of shadowing-effects by establishment of a U-shape. In addition, the charging was reduced by deposition of a platinum coating, fine tuned electron beam parameters and a method for charge neutralisation.

Establishment of a U-shape was the first step towards optimised imaging. The U-shape eliminated the shadowing-effects from surrounding walls of the cross-section surface. It did also reveal the full cross-section surface from obscuring material in front of the cross-section. The establishment of the U-shape did also involve deposition of a protective platinum coating ontop of the U-shape, this coating reduced charging. Table 1 shows the ion and electron beams parameters that have been used to establish the U-shape.

Table 1. Summary of the ion and electron beam parameters to establish a U-shape. Each process step is numbered and can be seen in Figure 7.

Process step	Beam Current	Beam Energy
1. Electron beam platinum deposition	260 pA	3 keV
1. Ion beam platinum deposition	200 pA	30 keV
2. Cross-section	3 nA	30 keV
3. Small trenches close to U-shape	3 nA	30 keV
4. Big trench in front of cross-section	40 nA	30 keV
5. Fiducial markers	2 nA	30 keV
6. Cleaning cross-section	1 nA	30 keV

The charging was further reduced by fine tuning the electron beam parameters. It was carried out by vary the energy until as little charging as possible was noticed while sustaining sufficient detector signal. The starting electron beam energy was chosen to be 2 keV, based upon the rule of thumb that the primary beam energy for no charging of poorly conductive materials lies within 2 keV-5 keV, depending on the material (Goldstein, 2003). By this experimental approach, the optimised electron beam energy was found to be 700 eV. If the electron beam energy was selected below 700 eV, less charging was observed, however too poor signal was received. If the electron beam energy was selected above 700 eV, the signal was improved. However, accumulation of local charges was observed which increased with longer exposure time. Next step was to optimise the electron beam current. The electron beam current was optimised with same approach as for the electron beam energy. The optimised electron beam current corresponded to minimum beam current that could be chosen, which was 1 pA.

Charge neutralisation using carbon gas was also used to reduce charging. The gas injection system from TESCAN was used. Cross-sectioning artefacts was present if the carbon gas was injected during milling, hence the gas was only injected prior to the electron beam imaging. The charge neutralisation procedure was carried out as followed. Carbon gas was injected into the chamber during 5 seconds by opening the carbon gas valve. The valve was closed after 5 seconds where upon imaging with reduced charging could be performed. This

was incorporated in the automatic slice and imaging procedure by pausing after each slicing. Therefore, the slice and imaging procedure resulted in a semi-automatic procedure. It was observed that the distance between the specimen and the valve opening played an important role. If the valve opening was too close to the specimen, curtaining was present. If the valve opening was too far away from the specimen, no charge neutralisation occurred. The optimised distance was experimentally tried out and was found to be by retracting the valve for 10 seconds from its inserted end position.

The 2D image stacks were obtained by using the ion beam for serial sectioning with slice thickness 50 nm for 10 μm depth (z). The width of the cross-section was 45 μm and the height 35 μm. The cross-section surface was imaged utilising a mid-angle BSE detector with scan speed 2 μs/pixel and 10 nm pixel size. The electron beam parameters used for imaging was 700 eV and 1 pA. Figure 9 shows one image of each cross-section of the porous polymer films where a) HPC22, b) HPC30 and c) HPC45. The view field of each cross-section image is 30 μm x 20 μm.

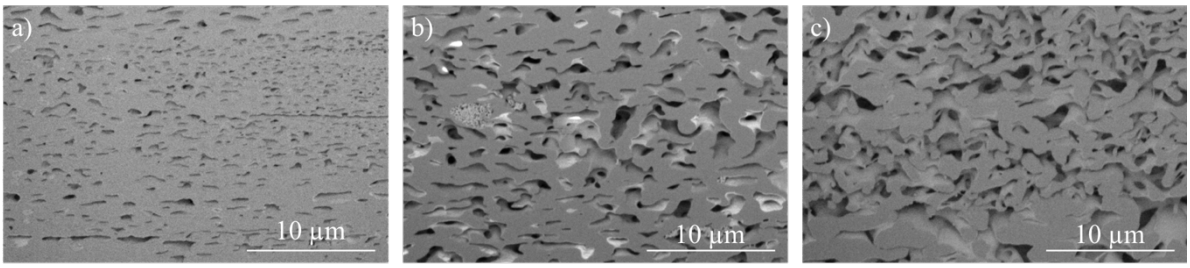

Figure 9. SEM mid-angle BSE images of cross-sections of porous polymer films. The view field of each image is 30 μm x 20 μm. The porous ethyl cellulose matrix is revealed in a) HPC22, b) HPC30 and c) HPC45.

3D VISUALISATION OF POROUS MICROSTRUCTURE SEGMENTATION USING SELF-LEARNING BINARISATION ALGORITHM

The 200 2D sequential images obtained by FIB-SEM tomography were aligned and cropped to 3000x2000 pixels using the software ImageJ (Schneider *et* al., 2012). The 3D reconstruction of the material requires segmentation of the solid and pore phases in the 2D images. However, each 2D image contains sub-surface information i.e. information about the structure in subsequent slices. This fact makes segmentation particularly challenging by introducing e.g. intensity overlaps. The first attempt was to use global thresholding (Efford *et* al., 2000) for segmentation, but the results were found non-satisfactory with no clear distinction between pore and a matrix. Instead, a machine learning-based method as used. Based on manual segmentation in 100 randomly placed square regions, each of size 256x256 pixels (corresponding to 0.5% of the full data, but nevertheless taking about 2 days to manually segment), a random forest classifier was trained to perform classification into one of two possible classes, matrix or pore. The trained classifier was subsequently used for segmentation of the full data set. The results from the segmentation algorithm can be seen in Figure 10. SEM mid-angle BSE images of the cross-sections are shown in the left column in Figure 10 a), c) and e). The corresponding binarised images are shown in the column to the right in Figure 10 b), d) and f). The view field of each cross-section is 30 μm x 20 μm.

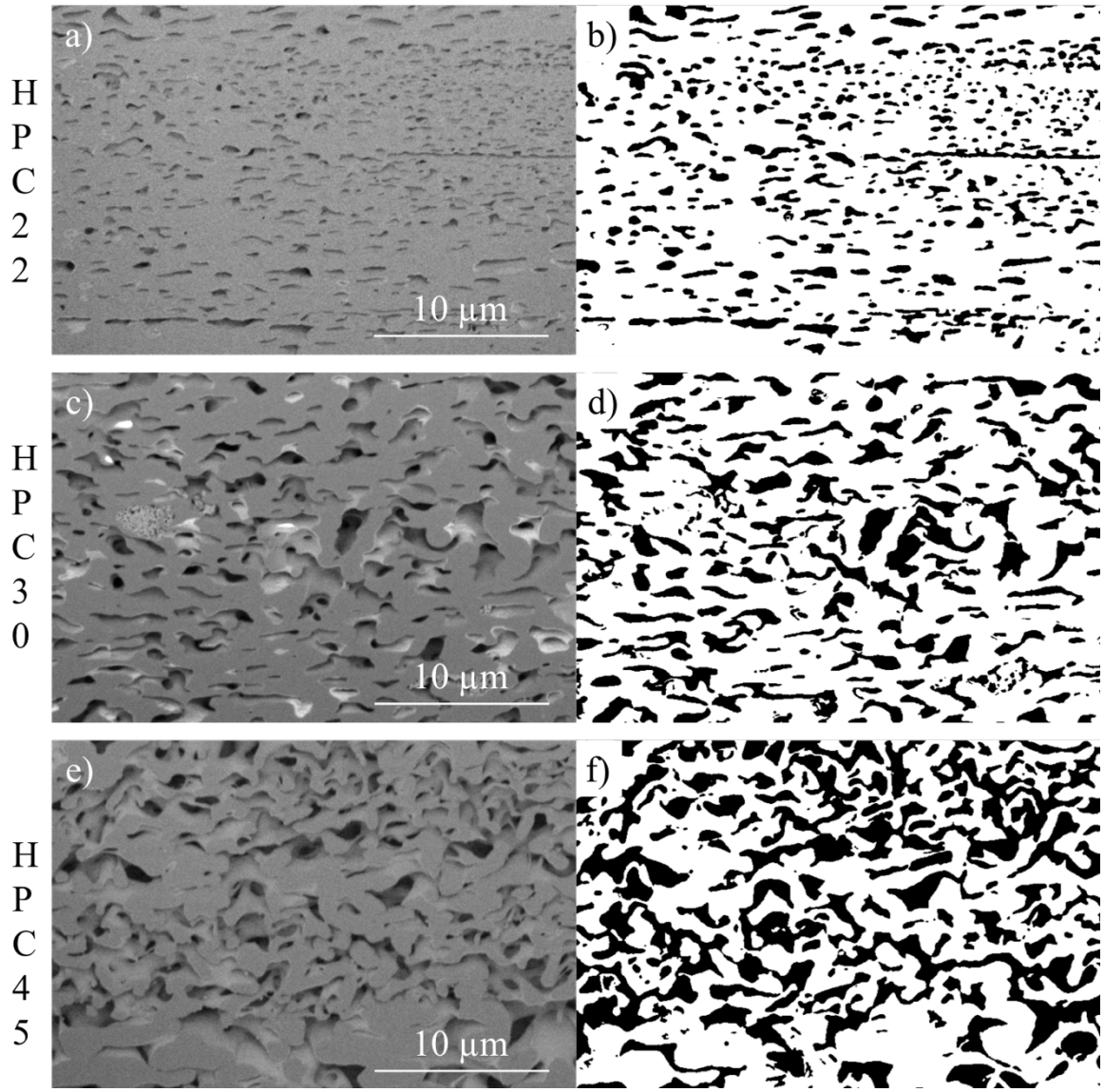

Figure 10. SEM mid-angle BSE cross-sectional images and corresponding binarised images. The left column shows SEM mid-angle BSE cross-sectional images of the three porous polymer films a) HPC22, c) HPC30 and e) HPC45. The column to the right shows the corresponding binary images to b) HPC22, d) HPC30 and f) HPC45.

3D reconstructions were done by importing the binary 2D image stacks into the software ORS Visual (Object Research Systems (ORS), Montreal, Canada). Figure 11 shows the SEM mid-angle BSE image stacks in the column to the left where a) HPC22, d) HPC30 and g) HPC45. The column in the middle in Figure 11 shows the 3D reconstruction of the porous network for b) HPC22, 3) HPC30 and h) HPC45. The column to the right in Figure 11 shows the porous EC matrix in 3D where c) HPC22, f) HPC30 and i) HPC45.

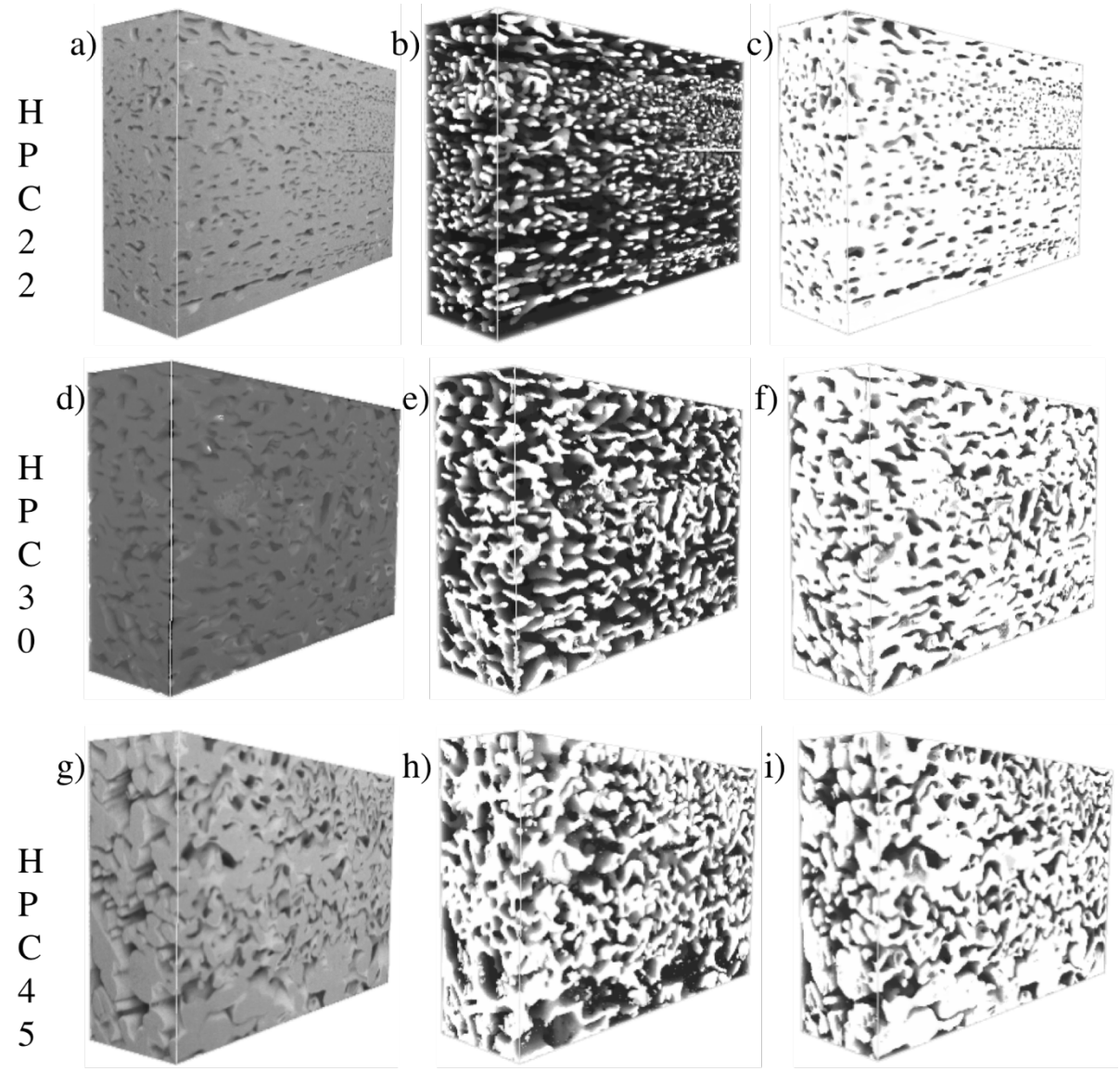

Figure 11. FIB-SEM mid-angle BSE image data sets and 3D reconstructions of porous network and porous EC matrix. The column to the left shows the SEM mid-angle BSE image stacks, the column in the middle shows the porous network in 3D and the column to the right shows the porous EC matrix in 3D. The three specimens are a-c) HPC22, d-f) HPC30 and g-i) HPC45.

ALGORITHM FOR SELECTING INDIVIDUAL PORES

The tortuosity, which measures the relative length of paths through the pore system, was utilised to identify paths of individual pores through the films. All paths from the same films that were considered started at the same pore. The algorithm that was utilised to extract these pores works as follows: All points in the pore system are associated with its geodesic path G, which is the shortest path through the pore system, which starts at the inlet pore, ends at the outlet and passes through the point. Corresponding to G is the tortuosity, $\tau = \frac{l(G)}{L}$, where $l(G)$ is the length of the path G and L is the length of the pore structure. The points of the pore system are divided into three categories, shortest, intermediate and longest geodesic path. The shortest category consists of all points with the lowest tortuosity, i.e. the points along the shortest path that starts at the inlet pore, the intermediate category consists of points with 15%-50% tortuosity, and the long category consists of points with 70%-90% tortuosity. The algorithm returns the shortest, intermediate and long geodesic paths. A randomly chosen point of the intermediate category of the long category returns the corresponding geodesic path associated with that point. The computation of the tortuosities τ and the geodesic paths G were implemented using Matlab's function *bwdistgeodesic* (Matlab, 2017).

INTERCONNECTIVITY OF ONE CHOSEN PORE AND ITS SHORTEST, INTERMEDIATE AND LONGEST PATHS

The tortuosity has been determined for three leached EC/HPC films with different porosities. The tortuosity value describes how much longer the pore paths are compared to the shortest possible path which is τ=1. Three tortuosity intervals are determined to represent the shortest, intermediate and longest paths. The shortest (a), intermediate (b) and longest (c) paths in leached HPC22, HPC30 and HPC45 are shown in 3D in Figures 12, 13 and 14, respectively. The front views give information about the pore paths morphologies in the cross-sectional plane while the side views provide information about the pore paths morphologies in the depth. The tortuosity values for each category and film are summarised in Table 2.

Table 2. Summary of tortuosity values for leached EC/HPC films.

Tortuosity / Film	HPC22	HPC30	HPC45
Shortest paths	2.37	1.16	1.07
Intermediate paths	2.63	1.24	1.17
Longest paths	4.14	1.84	1.62

The chosen pore and its shortest, intermediate and longest paths within leached HPC22 is shown in Figure 12. The shortest paths seen in Figure 12a), τ=2.37, are not widely wiggled through the porous network, which can be seen in the front view. However, the side view reveals that the pore paths are wiggled in the depth direction. The intermediate paths seen in Figure 12b), τ=2.63, are more spread out through the porous network which can be seen in the front view. The intermediate paths are also partly wiggled. From Figure 12c), it is shown that the longest paths in HPC22, τ=4.14, are spread out and wiggled.

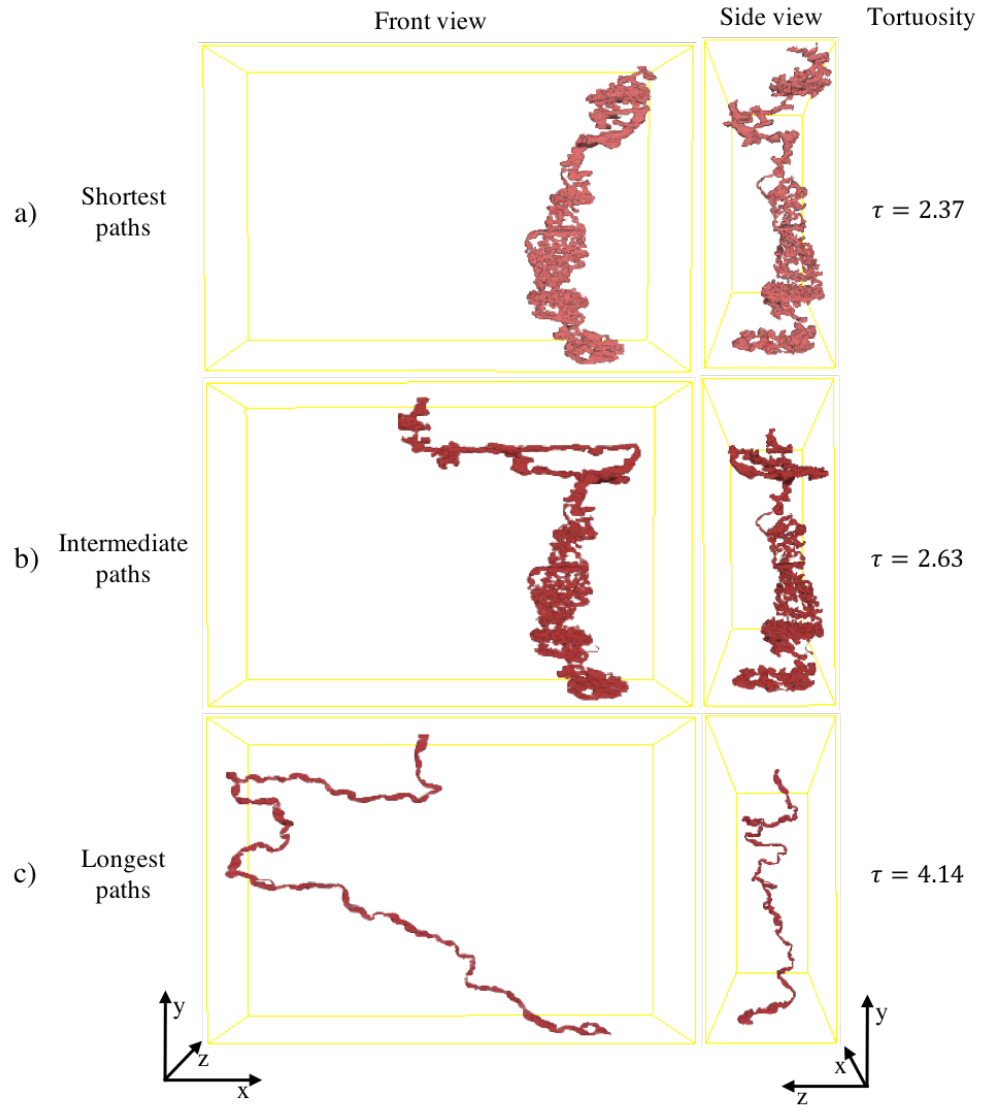

Figure 12. 3D visualisation in front view and side view of shortest, intermediate and longest pore paths for leached HPC22. Where a) shortest pore paths τ=2.37, b) intermediate pore paths τ=2.63 and c) longest pore paths τ=4.14.

The chosen pore and the different lengths of the pore paths within HPC30 can be seen in Figure 13. The shortest paths for HPC30 is shown in Figure 13a), τ=1.16, are relatively straight from bottom to top, seen from both the front and side views. The intermediate paths seen in Figure 13b), τ=1.24, are more wiggled compared to the shortest paths. It is observed that the longest paths seen in Figure 13c), τ=1.8.4, after the point that defines the geodesic path, i.e. the point for which this is the shortest path through the pore structure.

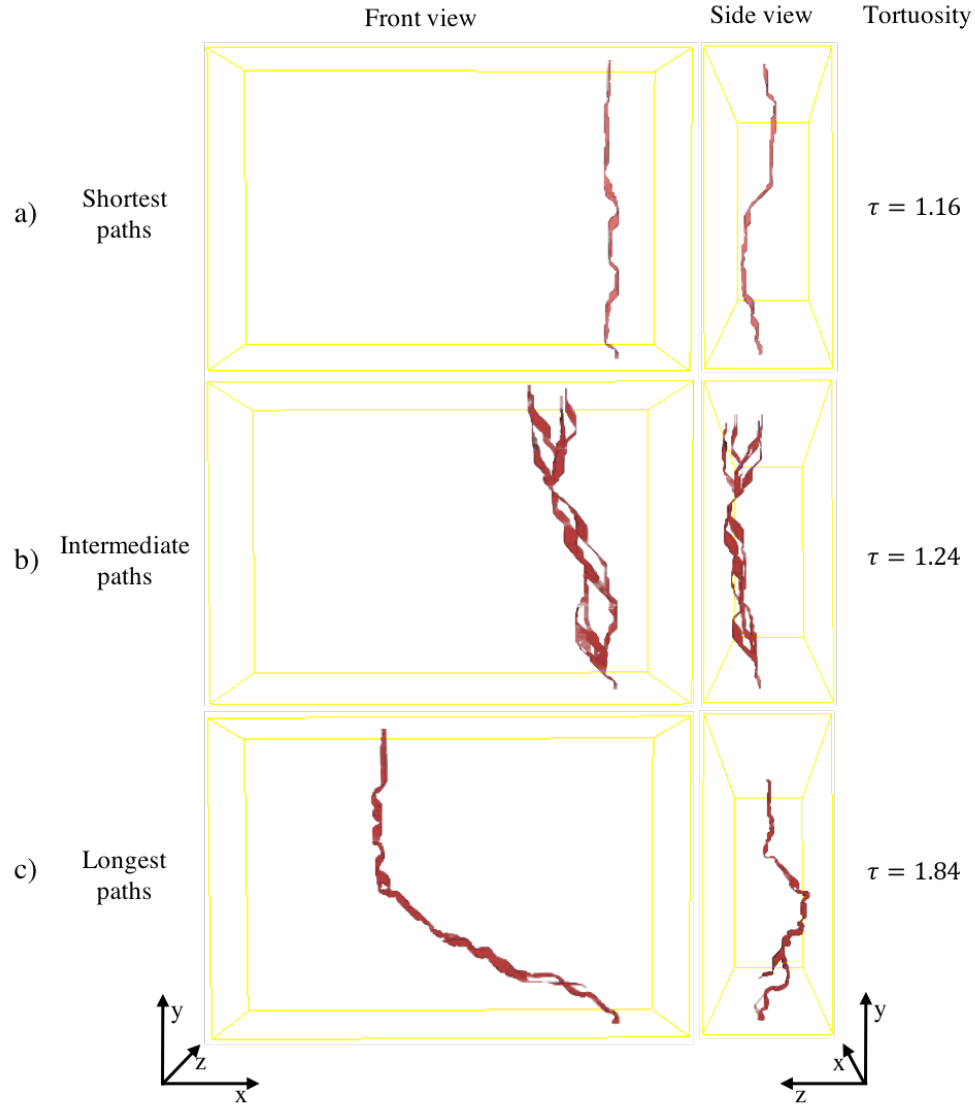

Figure 13. 3D visualisation in front view and side view of shortest, intermediate and longest pore paths for leached HPC30. Where a) shortest pore paths τ=1.16, b) intermediate pore paths τ=1.24 and c) longest pore paths τ=1.84.

Regarding the pore paths for leached HPC45, which can be seen in Figure 14, it is clear that the paths are not wiggled through the porous network. The shortest paths seen in Figure 14a), τ=1.07, are more or less straight paths from the inlet to the outlet of the pore. The intermediate paths seen in Figure 14b), τ=1.17, are relative straight as well and not widely wiggled. The case is similar case for the longest paths within HPC45 in Figure 14c), τ=1.62

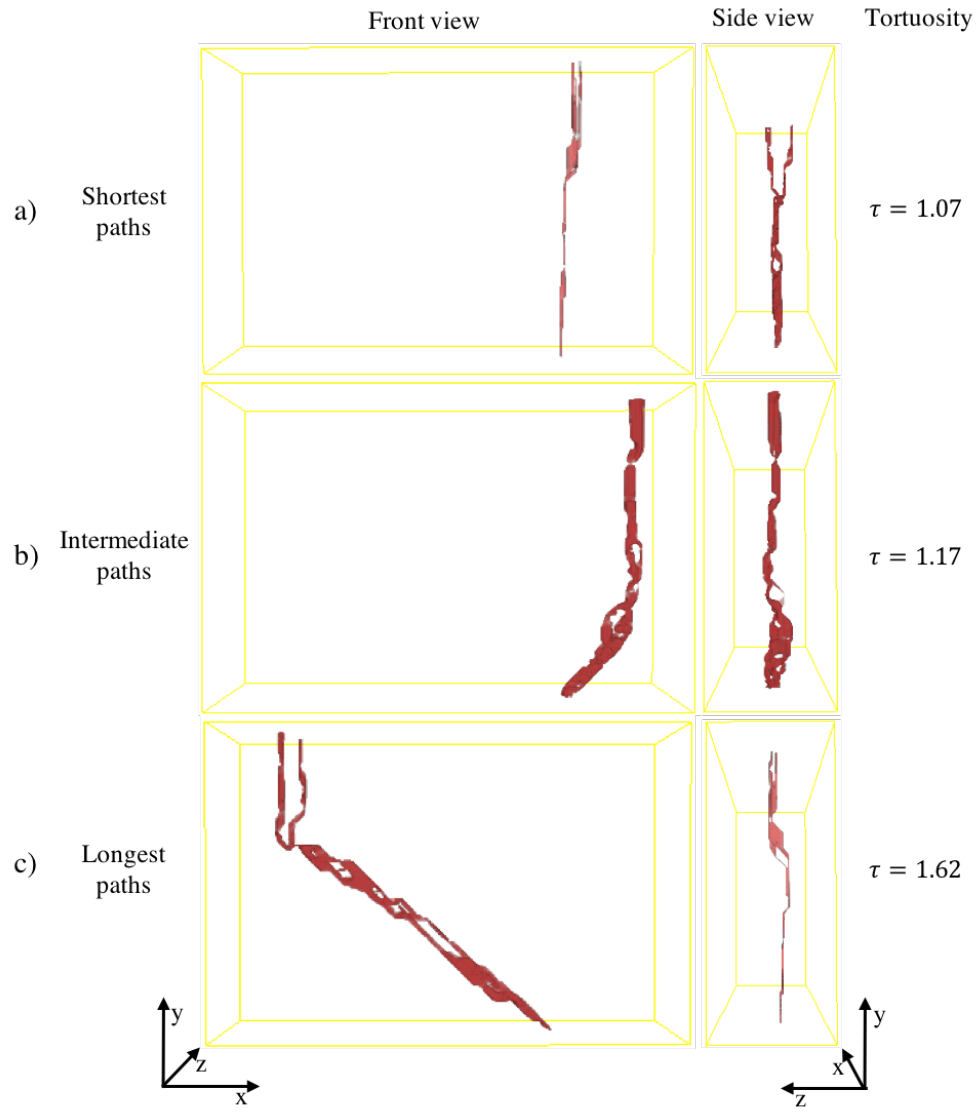

Figure 14. 3D visualisation in front view and side view of shortest, intermediate and longest individual pore paths for leached HPC45. Where a) shortest pore paths τ=1.07, b) intermediate pore paths τ=1.17 and c) longest pore paths τ=1.62.

INTERCONNECTIVITY COMPARISON OF INTERMEDIATE AND LONGEST PATHS IN HPC22, HPC30 AND HPC45

It is known from previous work that there is a percolation onset around 22 volume percentage of HPC (Marucci *et* al., 2013). A comparison of the interconnectivity within the films HPC22, HPC30 and HPC45 have been done by randomly choosing 5 of the intermediate and longest paths. These 5 randomly chosen intermediate and longest paths are visualised in 3D in Figure 15 and Figure 16, respectively. The intermediate and longest tortuosity intervals are summarised in Table 3. HPC22 has the highest tortuosity values in both the intermediate and longest tortuosity intervals. HPC30 has lower tortuosity values than HPC22 but higher than HPC45. It is observed that HPC45 always has the lowest tortuosity values.

Table 3. Summary of the tortuosity intervals for 5 randomly chosen paths in HPC22, HPC30 and HPC45. The τ values in the brackets represents the lowest and highest tortuosity values.

Tortuosity / Film	HPC22	HPC30	HPC45
Intermediate paths	[2.51, 2.92]	[1.23, 1.48]	[1.13, 1.28]
Longest paths	[3.52, 4.14]	[1.82, 2.18]	[1.51, 1.84]

The comparison between 5 randomly chosen intermediate paths for HPC22, HPC30 and HPC45 can be seen in Figure 15 a-c), respectively. The intermediate paths for HPC22, $\tau \in [2.51, 2.92]$ are significantly longer than the intermediate paths for HPC30 and HPC45. It can be seen from the 3D reconstructions that the paths in HPC22 wiggle more than HPC30 and HPC45. In addition, it can be seen that the paths in HPC30 spread out more compared to HPC45. This is confirmed by the higher tortuosity values for HPC30 $\tau \in [1.23, 1.48]$ in comparison to the lower tortuosity values for HPC45 $\tau \in [1.13, 1.28]$. Besides the wiggling, there is also a bottleneck in HPC22, at about one third of the length of the specimen from the top surface in the y-direction, at which all paths intersect.

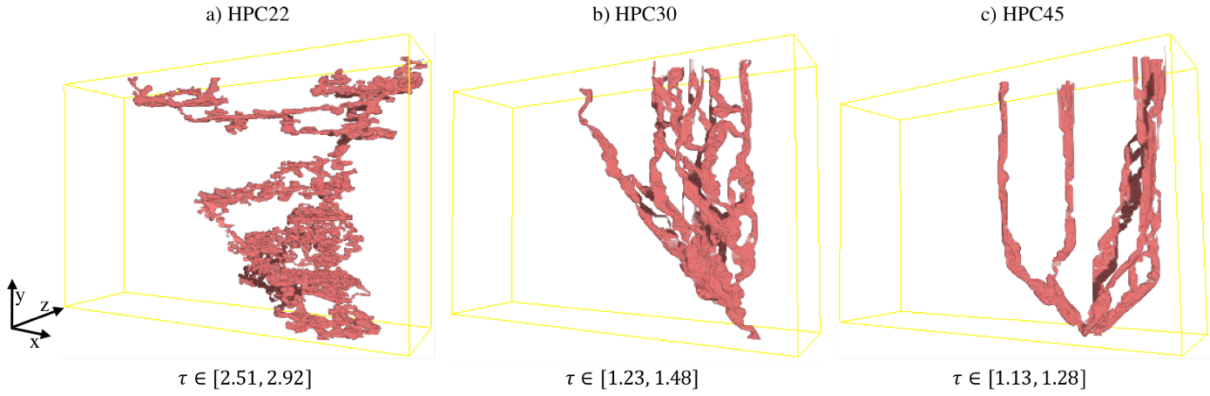

Figure 15. 3D visualisation of 5 randomly chosen intermediate paths for a) HPC22 with $\tau \in [2.51, 2.92]$, b) HPC30 with $\tau \in [1.23, 1.48]$ and c) HPC45 with $\tau \in [1.13, 1.28]$. The values in brackets are the lowest and the highest tortuosity values.

The comparison between 5 randomly chosen long paths for HPC22, HPC30 and HPC45 can be seen in Figure 16 a-c), respectively. It can be seen from Figure 16a) that the paths in HPC22 are highly wiggled throughout the whole porous network and the tortuosity values are $\tau \in [3.52, 4.14]$. It is revealed from Figure 16b) that the long paths in HPC30 are not as highly wiggled as for HPC22. The tortuosity for the long paths for HPC30 vary between $\tau \in [1.82, 2.18]$. Furthermore, it can be seen from Figure 16c) that the long paths for HPC45 are not as wiggled as in HPC30. The tortuosity for the long paths for HPC45 vary between $\tau \in [1.51, 1.84]$. The same behaviour as for the intermediate paths can be observed here for HPC22, with a strong bottleneck effect. There seems to be two bottlenecks at the same height, at about one third from the top surface in the y-direction. Additionally, the long paths essentially coincide at the same positions at the top as the intermediate paths, also indicating strong bottleneck effects.

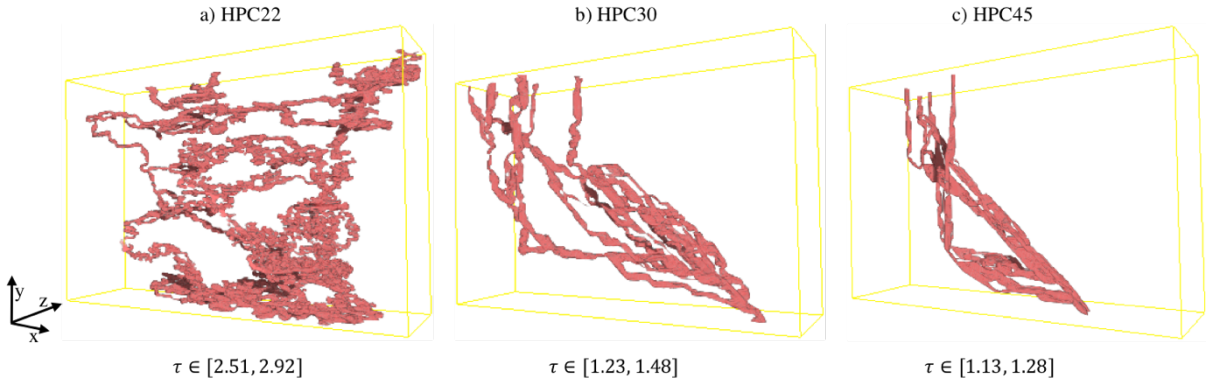

Figure 16. 3D visualisation of 5 randomly chosen longest paths a) HPC22 with $\tau \in [3.52, 4.14]$, b) HPC30 with $\tau \in [1.82, 2.18]$ and c) HPC45 with $\tau \in [1.51, 1.84]$. The values in brackets are the lowest and the highest tortuosity values.

Chapter 5

- "When the struggle gets real the changes come along"

DISCUSSION

The FIB-SEM tomography parameters have been optimised for porous and poorly conductive soft materials. The work has been carried out on leached EC/HPC films. 3D reconstructions are presented for three films with different EC/HPC volume percentage. Based on the work and the observations a general approach for the optimisation of milling and imaging parameters is presented and discussed. First, we introduce a protocol for optimisation of the ion beam parameters for milling to reduce cross-sectioning artefacts, such as curtaining and redeposition. Thereafter follows the optimisation of imaging parameters which involves elimination of shadowing-effects by a U-shape. In addition, charging is reduced by applying the developed protocol of how to optimise the electron beam parameters as well as by deposition of a platinum coating and a method for charge neutralisation. A self-learning algorithm for binarisation of the 2D image stacks for an automatic and time efficient 3D reconstruction is introduced. Furthermore, the interconnectivity of the pore paths has been visualised in 3D based upon tortuosity calculations.

OPTIMISATION OF ION BEAM MILLING

The optimisation of the milling parameters was carried out by tuning the ion beam energy and current. The conclusion was that cross-sectioning artefacts such as curtaining or redeposition could be avoided at 30 keV provided that the ion beam current was fine tuned. In general, a high beam current is used for rough milling in order to remove large volumes time efficiently (Giannuzzi *et* al., 2005). In our case, we found that 40 nA fulfilled the requirement for rough milling. Depending on material structures this needs to be fine tuned. Next step was to remove redeposition and curtaining. Previous work has shown that the curtaining effect is governed both by the ion beam current and structural inhomogeneity of the specimen (Walley *et* al., 1971; Suzuki, 2002). Hence, a platinum coating was deposited on the surface, both to protect the surface from the ion beam as well as to reduce the sputter rate difference caused by the surface roughness. The tuning of the ion beam current for reduction of redeposition and curtaining was started from a low current followed by a stepwise increase. This was done in order to find an optimal current giving the combination of fast milling and minimised redeposition and curtaining, which in our case was 1 nA.

OPTIMISATION OF ELECTRON BEAM IMAGING

The optimisation of the imaging parameters included reduction of shadowing-effects caused by surrounding material (Holzer *et* al., 2004). Hence, establishment of a U-shape was required. The U-shape successfully eliminated the shadowing-effects allowing the full cross-section surface to be imaged.

During the imaging of porous and poorly conductive materials using the electron beam, charging effects needs to be reduced. The charging is related to the electron yield which depends on the primary electron beam energy. If the beam energy is chosen so that the electron yield is lower than 1, more electrons are impinging the surface than leaving, thus a negative charge accumulation results in the specimen. If the energy is chosen so that the electron yield is higher than 1, more electrons leave the specimen compared to the impinging, resulting in a positive charge accumulation. There are two cross-over points where the primary beam energy gives an electron yield equal to 1 (Goldstein, 2003). At low energy below the first cross-over there is a negative charge accumulation. At energies between the two cross-overs there is a positive charge accumulation. For soft materials, the low energy cross-over point occurs in the energy range of 0.5 keV – 2 keV and the high cross-over point at 2 keV - 5 keV (Goldstein, 2003). The starting electron beam energy was chosen to 2 keV since higher beam energies resulted in too much charging. Charging was present at 2 keV, hence the energy beam was lowered stepwise with steps of 0.1 keV until as little charging as possible was achieved with still sufficient detector signal. The charging had been reduced as well as sufficient detector signal was obtained. 0.7 keV was found to be the optimised beam energy for imaging. Depending on material structures this need to be fine tuned. The electron beam current was optimised with the same stepwise lowering approach as for the ion beam, with the starting current of 3 nA. The optimised electron beam current corresponded to minimum beam current that could be chosen, which was 1 pA.

Even though charging was reduced by optimising the electron beam parameters, charging was still present at smaller regions over the cross-section surface. This charging was further reduced by charge neutralisation by injection of a carbon gas (Schulz *et* al., 2009; Robinson, 1975; Moncrieff *et* al., 1978; Stokes, 2008). It was observed that the distance between the opening of the gas injection system and the specimen was important and had to be optimised.

2D IMAGE STACK BINARISATION

The presence of pores added additional challenges regarding segmentation. While fully dense materials provide a planar cross-section, pores expose surface area beneath the planar cross-section surface as well. This sub-surface pore information and the varying intensity from the sub-surface areas give rise to intensity overlaps which complicate the data processing. It was found that a first-resort method like global thresholding was non-satisfactory, not providing a clear distinction between matrix and pore. A better method to distinguish between matrix and pore would be to manually mark the pores, but this is extremely time consuming. Our solution was to manually segment approximately 0.5 % of the full data and use that to train a classification algorithm, with which the full data set could be satisfactory segmented and binarised.

3D VISUALISATION OF INTERCONNECTIVITY

The interconnectivity of the pore paths within the EC/HPC films has been visualised in 3D. It has been observed from the 3D reconstructions that both leached HPC30 and HPC45 comprised of less wiggled porous paths compared to leached HPC22. This can be related to the percolation onset discovered from previous studies performed on these films (Marucci *et* al., 2009). The amount of leached HPC and the water permeability were lower below 22 volume percentage and higher above the percolation onset.

A trend is observed where HPC22 is much more wiggled compared to HPC30 and HPC45, for all three path categories. The paths in HP22 also seem to behave differently compared to the other two films. There are significant bottlenecks in HPC22, where many of the paths pass through the same position of the pore structure. One reason why the pore paths are qualitatively different in HPC22 is that the structure is close to the percolation onset. HPC30 and HPC45 appear more similar in their porous paths, with less wiggled and more straight porous paths. This could be explained by their structures being far beyond the percolation onset.

It should also be pointed out that the shortest paths for HPC30 and HPC45 appear as more or less straight paths from the bottom to the top. However, there does exist a difference between HPC30 and HPC45 when it comes to the tortuosity values. The intermediate and longest paths for HPC30 are 1.24 and 1.84 while they are 1.17 and 1.62 for HPC45. This implies that higher volume percentage of HPC result in less wiggled structure and lower tortuosity values.

Chapter 6

-" If you want to accomplish something you never have done before, then you must do something that you never have done before".

CONCLUSIONS AND OUTLOOK

A general protocol for optimisation of FIB-SEM tomography parameters for porous and poorly conductive soft materials has been developed. It optimises the reduction of cross-sectioning artefacts, eliminates shadowing-effects and reduces charging. In addition, it handles the sub surface and intensity overlap problems in the binarisation stage of the 3D reconstruction. The cross-sectioning artefacts, redeposition and curtaining, were reduced by deposition of a platinum coating and optimisation of the ion beam energy and current. The shadowing-effects were eliminated by establishing a U-shape. The charging problem was reduced by deposition of the platinum coating, optimisation of the electron beam energy and current as well as charge neutralisation using a carbon gas. The sub surface information in the images caused complications for the binarisation step of the 3D reconstruction. A self-learning algorithm for binarisation of the 2D image stacks for an automatic and time efficient 3D reconstruction is introduced. This approach for optimisation of the FIB-SEM tomography parameters data has been demonstrated on leached EC/HPC porous polymer films with poor conductivity.

The 3D reconstructions of the EC/HPC films were quantitatively evaluated with respect to tortuosity. The interconnectivity of the pore paths was visualised in 3D. A trend was observed where an increased volume percentage of HPC resulted in a lower tortuosity value.

The next step in the studies of the EC/HPC films is to correlate the microstructure to mass transport through the porous network. The quantitative data will be used for flow simulations. A new geometry with EC/HPC films in pellets with a drug core will be introduced and evaluated applying our optimised FIB-SEM tomography approach. Moreover, the porous network developed during manufacturing by phase separation. New information about the interface between the two immiscible polymers and the phase separation mechanism can be obtained by transmission electron microscopy.

References

ANDERSON, R.U., MOBLEY, D., LANK, B., SALTZSTEIN, D., SUSSET, J. & BROWN, J.S. (1999). Once daily controlled versus immediate release oxybutynin chloride for urge urinary incontinence. *The Journal of UrologY.* **161**(6), 1809-1812.

ANDERSSON, H., HJÄRTSTAM, J., STADING, M., VON CORSWANT, C. & LARSSON, A. (2013). Effects of molecular weight on permeability and microstrucutre of mixed ethy-hydroxypropyl-cellulose films. *European Journal of Pharmaceutical Sciences*. **48,** 240-248.

ANDERSSON, H., HÄBEL, H., OLSSON, A., SANDHAGEN, S., VON CORSWANT, C., HJÄRTSTAM, J., PERSSON, M., STADING, M. & LARSSON, A. (2016). The influence of the molecular weight of the water-souble polymer on phase-separated films for controlled release. *International Journal of Pharmacerutics.* **511**, 223-235.

ANDERSSON, H.M, MARUCCI, M., HÄRDELIN, L., HJÄRTSTAM, J., STADING, M., VON CORSWANT, C. & LARSSON, A. (2018). New insights in the influence of manufacturing conditions and molecular weight on phase-separated films intended for controlled release. *International Journal of Pharmaceutics*. 536, 261-271.

BASSIM, N.D., DE GREGORIO, B.T., KILCOYNE, A.L.D., SCOTT, K., CHOU, T., WIRICK, S., CODY, G. & STROUD, R.M. (2011). Minimizing damage during FIB sample preparation of soft materials. *Journal of Microscopy*. **245**, pp. 288-301.

BASSIM, N., SCOTT. & GIANNUZZI, L. A. (2014). Recent Advances in Focused Ion Beam Technology and Applications, *MRS Bull,* 39, pp. 317-325.Inkson, B.J., Mulvihill, M. & Möbus, G. 3D determination of grain shape in a FeAl-based nanocomposite by 3D FIB tomography. *Scripta Mater* **45**. 753-758.

BLAYVAS, I., BRUCKSTEIN, A. & KIMMEL, R. (2006). Efficient computation of adaptive threshold surfaces for image binarization. *Pattern Recognition*. **39**, 89-101.

CANTONI, M. & HOLZER, L. (2014). Advances in 3D Focused Ion Beam Tomography, *MRS Bull,* 354-360.

DAVENPORT, H.W. (1982). *Physiology of the Digestive Tract*. Year Book Medical Publishers: Chicago.

DEERINCK, T.J., BUSHONG, E.A., LEV-RAM, V., SHU, X., TSIEN, R.Y. & ELLISMAN, M.H. (2010). Enhancing serial block-face scanning electron microscopy to enable high resolution 3-D nanohistology of cells and tissues. *Microscopy and microanalysis*. **16** (2), 1138-1139.

DE WINTER. D.A.M., SCHNEIJDENBERG, C. T. W. M., LEBBINK, M. N., LICH, B., VERKLEIJ, A. J., DRURY, M. R. & HUMBEL, B. M. (2009). Tomography of Insulating Biological and Geological Mateirals Using Focused Ion Beam (FIB) Sectioning and Low-kV BSE Imaging. *Journal of Microscopy.* **233**(3), 372-383.

DIVOLL, M., GREENBLATT, D.J., OCHS, H.R. & SHADER, R.I. (1983). Absolute Bioavailability of Oral and Intramuscular Diazepam: Effects of Age and Sex. *Anasthesia & Analgesia.* **62**(1), 1-8.

DROBNE, D., MILANI, M., LESER. V & TATTI, F. (2007). Surface Damage Induced by FIB Milling and Imaging of Biological Samples is Controllable. *Microscopy Research and Technique* 70, 895-903.

DUBOCHET,J., ADRIAN, M., CHANG, J-J., OMO, J-C., LEPAULT, J., MCDOWALL, A.W. & SCHULTZ, P. (1988). Cryo-electron microscopy of vitrified specimens. *Quarterly Review of Biophysics.* **21**(2), 129-228.

EDSBÄCKER, S., LARSSON, B.B., LARSSON, P., LUNDIN, P., NILSSON, Å., ULMIUS, J. & WOLLMER, P. (2003). A pharmacoscintigraphic evaluation of oral budesonidegiven as controlled-release (Entocort) capsules. *Alimentary Pharmacology & Therapeutics.* **17**(4), 525-536.

EFFORD, N. Digital image processing. (2000). New York: Addison Wesley.

FAGER, C. & OLSSON, E. (2018). Nanotechnologies in Preventive and Regenerative Medicine. V. Uskokovic and D. P. Uskokovic. *Soft Materials and Coatings for Controlled Drug Release.* Netherlands: Elsevier. 244–259.

FELTON, L.A. & TIMMINS, G.S. (2006) A Nondestructive Technique to Determine the Rate of Oxygen Permeation into Solid Dosage Forms. *Pharmaceutical Development and Technology.***11,** 141-147.

FELTON, L.A. (2007). Characterization of Coating Systems. *AAPS PharmSciTech*. **8**(4).

GIANNUZZI, L.A. & STEVIE, F.A. (2005). *Introduction to focused ion beams*: Instrumentation, theory, techniques and practise. USA: Springer

GOLDSTEIN, J., NEWBURY, D., JOY, D., LYMAN, C., ECHLIN, P., LIFSHIN, E., SAWYER, L. & MICHAEL, J. (2003). Scanning electron microscopy and x-ray microanalysis 3rd edition. (New York: Plenum)

GRUBER, P., LONGER, M.A. & ROBINSON, J.R. (1987). Some biological issues in oral, controlled drug delivery. *Advanced Drug Delivery Reviews.* **1**(1), 1-18.

HEYMANN, J.A., HAYLES, M., GESTMANN, I., GIANUZZI, L.A., LICH, B. & SUBRAMANIAM, S. (2006). Site-specific 3D imaging of cells and tissues with a dual beam, microscope. *Journal of Structural Biology* **155**, 63-73.

HOLZER, L., INDUTNYI, F., GASSER, P.H., MUCH, B. & WEGMANN, M. (2004). Three-dimensional analysis of porous $BaYiO_3$ ceramics using FIB nanotomography. *Journal of Microscopy.* **216**, 84-95.

HUTTON, J.T. & MORRIS, J.L. Morris. (1992). Long-acting carbidopa-levodopa in the management of moderate and advanced Parkinson's disease. *Neurology.* **42**(1), 51-56
INKSON, B.J., STEER, T., MOBUS, G. & WAGNER, T. (2001). Subsurface nanoindentation deformation of Cu-Al multilayers mapped in 3D by foused ion beam microscopy. *Journal of Microscopy.* **201**, 256-269.

JANSSON, A., NAFARI, A., SANZ-VELASCO, A., SVENSSON, K., GUSTAFSSON, S., HERMANSSON, A-H & OLSSON , E. (2013). Novel Method for Controlled Wetting of Materials In the Environmental Scanning Electron Microsope. *Microscopy and Microanalysis.* **19**, pp. 30-37.

JOERGENSEN, P.S., HANSEN, K.V., LARSEN, R. & BOWEN, J.R .(2010). A framework for atuomatic segmentation in three dimensions of microstructural tomography data. *Ultramicroscopy*. 110, 216-228.

JONES, R.A.L. & RICHARDS, R.W. (1999). Polymers at surfaces and interfaces, Cambridge, Univeristy Press, Cambridge, UK.

KIRK, E.C.G., WILLIAMNS, D.A. & AHMED, H. (1987) in situ microsectioning and imaging of semiconducttor devices. *Insitute of Physics Conference Series*. **87**, 691-696.

KLEIN, E. (2002). The role of extended-release benzodiazepines in the treatment of anxiety: a risk-benefit evaluation with a focus on extended-release alprazolam. *The journal of clinical psychiatry.* **63**(14), 27-33.

LANGER, R. & PEPPAS, N. (1983). Chemical and Physical Structure of Polymers as Carriers for Controlled Release of Bioactive Agents: A Review. *Macromolecular Science Part C.* **23**(1), 61-126.

LANGER, R. & PEPPAS, N. (2003). Advances in Biomaterials, Drug Delivery, and Bionanotechnology. *American Institute of Chemical Engineers Journal.* **49**(12), 2990-3006.

LECOMTE, F., SIEPMANN, J., WALTHER, M., MACRAE, R.J. & BODMEIR, R. (2003). Blends of Enteric and GIT-Insoluble Polymers Used for Film Coating: Physicochemical Characterization and Drug Release Patterns, *Journal of Controlled Release.* **89**, 457-471.

MATLAB. Version R2017b. Natick, Massachusetts: The MathWorks Inc.; 2017.

MARUCCI, M., HJÄRTSTAM, J., RAGNARSSON, G., ISELAU, F. & AXELSSON, A. (2009). Coated Formulations: New Insights Into the Release Mechanism and Changes In the Film Properties with a Novel Release Cell. *Journal of Controlled Release*, **136**(3), 206-212.

MARUCCI, M., ARNEHED, J., JARKE, A., MATIC,H., NICHOLAS, M., BOISSIER, C. & VON CORSWANT, C. (2013). Effect of the Manufacturing Conditions On the Structure and Permeability of Polymer Films Intended for Coating Undergoing Phase Separation, *European Journal of Pharmaceutics and Biopharmaceutics.* **83**, pp. 301-306.

MONCRIEFF, D.A., ROBINSON, V.N.E. & HARRIS, L.B. (1978). Charge neutralisation of insulating surfaces in the SEM by gas ionisation. *Journal of Physics D: Applied Physics*. **11**, 2315-2325.

NARAYAN, K. & SUBRAMANIAM, S. (2015). Focused Ion Beams in Biology. *Nature Methods.* **12**, pp. 1021-1031.

NASTASI, M., MAYER, JW. & HIRVONEN, JK. (1996). *Ion-solid interactions: Fundamentals and applications.* Cambridge University Press, Great Britain.

OBJECT RESEARCH SYSTEMS (ORS), Montreal, Canada (2018)

RAWLINGS, J.M. & LUCAS, M.L. (1985). Plastic pH Electrodes for the Measurement of Gastrointestinal pH. *Gut*. **26,** 203-207.

RHODES, C.T. &PORTER, S.C. (1998). Coatings for Controlled-Release Drug Delivery Systems. *Drug Development and Industrial Pharmacy.* **24**(12), 1139-1154.

ROBINSON, V.N.E. (1974). The elimination of charging artefacts in the scanning electron microscope. *Journal of Physics E: Scientific Instruments*. **8**, 638-640.

SAKELLARIOU, P. & ROWE, R.C. (1995). Interactions in Cellulose Derivative Films for Controlled Drug Delivery. *Progress in Polymer Science*. **20**(5), 889-942.

SALZER, M., SPETTL, A., STENZEL, O., SMÅTT, J-H., LINDÉN, M., MANKE, I. & SCHMIDT, V. (2012). A two-stage approach to the segmentation of FIB-SEM images of highly porous materials. *Materials Characterization*. 69, 115-126.

SALZMAN, C., SHADER, R.I. GREENBLATT, D.J. & HARMATZ, J.S. (1983). Long vs Short Half-life Benzodiazepines in the Elderly Kinetics and Clinical Effect of Diazepam and Oaxzepam. *Archives of Generally Phychitry.* **40**(3), 293-297.

SCHNEIDER, C.A., RASBAND, W.S. & ELICEIRI, K.W. (2012). NIH Image to ImageJ: 25 years of image analysis. *Nature Methods.* **9**(7): 671-675.

SCHULENBERG, H., SCHWANITZ, B., KRBANJEVIC, J., LINSE, N., SCHERER G.G. & WOKAUN, A. (2011). 3D imaging of catalyst support corrosion in polymer electrolyte fuel cells. *The Journal of Physical Chemistry*. **115**, 14236–14243.

SCHULZ, H., ZEILE, U., STODOLKA, D & KAFT, D. (2009). Advantages of a Local Charge Compensation System for FIB/SEM Applications on Insulating Materials. *Microscopy and Microanalysis*. **15**(Suppl 2), pp. 332.

SELIGMAN, A.M., WASSERKRUG, H.L. & HANKER, J.S. (1966). A new staining method (OTO) for enhancing contrast of lipid-containing membranes and droplets in osmium tetroxide-fixed tissue with osmiophilic thiocarbohydrazide (TCH). *The Journal of Cell Biology.* **30**(2), 424-432.

SELIGER, R.L, WARD, J.W., WANG, V. & KUBENA, R.L. (1979). A high-inensity scanning ion probe with submicrometer spot size, *Applied Physics Letter*, **34** (5), 310-312

SIEPMANN, F., HOFFMANN, A., LECLERCQ, B., CARLING, B. & SIEPMANN, J. (2007). How to Adjust Desired Drug Release Patterns from Ethylcellulose-Coated Dosage Forms, *Journal of Controlled Release,* 119, 182-189.

SIEPMANN, F., SIEPMANN, J., WALTHER, M., MACRAE, R.J. & BODMEIER. (2008). Polymer Blends for Controlled Release Coatings, *Journal of Controlled Release.* **125**, pp. 1-15.

STOKSE, D., *RMS - Royal Microscopical Society : Principles and Practice of Variable Pressure : Environmental Scanning Electron Microscopy (VP-ESEM)*. (2008). West Sussex, UK: John Wiley & Sons Ltd.

SUBRAMANIAM, S., 2005. Bridging the Imaging Gap: Visualizing Subcellular Architecture with Electron Tomography. *Current Opinion in Microbiology.* **8**, pp. 316-322.

SUZUKI, E. (2002). High-resolution scanning electron microscopy of immunogold-labelled cells by the use of thin plasma coating of osmium. *Journal of Microscopy.* **208**, 153-157.

TANAKA,K. & MITSUSHIMA, A. (1984). A preparation method for observing intracellular structures by scanning electron microscopy. *Jounral of Microscopy.* **133**, 213- 222.

THIEDMANN,R., HASSFELD,H., STENZEL, O., KOSTER, L.J.A., OOSTERHOUT, S.D. & VAN BAVEL, S.S. (2011). A multisacle approach to the representation of 3D images, with application to polymer solar cells. *Image Anal Stereol.* **30**, 19-30.

WALLEY, P.A., WINEBERG, M. & BURDEN, M.ST J. (1971). The use of an electron beam evaporation source for electron microscope sample preparation. *Journal of Physics E: Scientific Instruments.* **4**, 501-504.

ZILS, S., TIMPEL, M., ARLT, T., WOLZ, A., MANKE, I. & TORH, C. (2010). 3D visualization of PEMFC electrode structures using FIB nanotomography. *Fuel Cells*. **10**, 966-972.